Acta Materialia 265 (2024) 119593

Contents lists available at ScienceDirect

Acta Materialia

journal homepage: www.elsevier.com/locate/actamat

Full length article

Synchrotron X-ray operando study and multiphysics modelling of the solidification dynamics of intermetallic phases under electromagnetic pulses

Ling Qin [a,b], Wenjia Du [a,c], Silvia Cipiccia [d,e], Andrew J. Bodey [d], Christoph Rau [d], Jiawei Mi [a,f,*]

[a] School of Engineering, University of Hull, East Yorkshire HU6 7RX, UK
[b] Department of Petroleum Engineering, University of Wyoming, Wyoming 82071, USA
[c] Department of Engineering Science, University of Oxford, Oxford OX1 3PJ, UK
[d] Diamond Light Source, Harwell Science and Innovation Campus, Didcot OX11 0DE, UK
[e] Department of Medical Physics and Biomedical Engineering, University College London, London WC1E 6BT, UK
[f] School of Materials Science & Engineering, Shanghai Jiao Tong University, Shanghai 200240, China

ARTICLE INFO

Keywords:
Synchrotron X-rays
Multiphysics modelling
Solidification dynamics
Intermetallic phases
Pulse magnetic fields

ABSTRACT

In this paper, we used synchrotron X-ray radiography and tomography to study systematically and in operando conditions the growth dynamics of the primary Al_3Ni intermetallic phases in an Al-15wt%Ni alloy in the solidification process with magnetic pulses of up to 1.5 T. The real-time observations clearly revealed the growth dynamics of the intermetallics in time scale from millisecond to minutes, including phase growth instability, side branching, fragmentation and orientation alignment under different magnetic pulse fluxes. A multiphysics numerical model was also developed to calculate the alternating and cyclic Lorentz forces and stresses acting on the Al_3Ni phases and the nearby melt due to the applied pulses. Combining the results of the operando experiments and modelling, for the first time, the differential forces between the growing Al_3Ni phases and the nearby melt were quantified. The forces can create slip dislocations at the growing crystal front which can further develop into nm and μm crystal steps for initiating phase branching. Furthermore, the magnitudes of the shear stresses are strongly related to the size, morphological and geometric features of the growing Al_3Ni phases. Dependent on the magnitude of the shear stresses, phase fragmentation could occur in a single pulse period or in multiple pulse periods via fatigue mechanism. This systematic research work elucidate some of the long-time debated hypotheses concerning intermetallic phases growth instability and phase fragmentation in pulse magnetic fields. The research establishes a robust theoretical framework for quantitative understanding of the intermetallic phase growth dynamics in solidification under pulse magnetic fields.

1. Introduction

An intermetallic compound in a metal alloy is a metallic phase consisting of two or more metallic elements with a unique crystalline structure [1–3]. These compounds are typically formed during the transition from the liquid to solid state, i.e., in the solidification processes. The thermal, convective and external physical fields applied into the solidification processes are the essential driving forces [4–6] for phase nucleation and growth. In addition, the inherent properties of the alloy, e.g., the anisotropy and/or interfacial energy of the solid-liquid interface, atomic diffusivity [7] and kinetic properties of atom attachment [8] also determine the nucleation and growth dynamics of an intermetallic phase. In terms of the external fields, ultrasonic, electrical current, and electromagnetic methods are the common methods employed in the solidification processes for manipulating or controlling the formation and growth of intermetallics [9–13] in different alloy systems. The general purpose is to achieve the beneficial size, morphology and distribution of the intermetallics for structural and functional properties control and/or performance enhancement. The application of an external field into a liquid metal can be realized by immersing specially-designed sonotrodes or electrodes directly into the liquid. In such case, it must withstand the high-temperature melt erosion [14]. Alternatively, the field can be applied via electromagnetic coupling in a non-contact manner, which is particularly useful for

* Corresponding author.
E-mail address: j.mi@hull.ac.uk (J. Mi).

https://doi.org/10.1016/j.actamat.2023.119593
Received 17 July 2023; Received in revised form 13 November 2023; Accepted 9 December 2023
Available online 14 December 2023

high-temperature or high-purity alloy melts [15].

Many studies have been conducted over the past few decades to develop efficient electromagnetic methods for liquid metal processing. For example, applying static magnetic fields [16,17] to dampen and control natural convection or melt flow fluctuations in continuous casting; using high-frequency alternating magnetic fields to improve superficial properties [15,18]; adopting low-frequency alternating magnetic fields for removing impurities [19–21]. In the solidification processes, the applied fields have been mainly for controlling the nucleation, growth and morphology of dendritic and intermetallic phases in different alloys [22–25], realising grain refinement [26,27] or phase alignment for targeted applications. In recent years, pulse electromagnetic fields (PMF) have gained recognition as a promising method for grain refinement in metal alloys. PMF has advantages in no excessive extra heat generation into the melt, no direct-contact contamination to the melt. PMF can generate short pulses (in ms duration) with high peak magnetic flux intensity and programable frequency [28–32]. The unique advantage of using much less energy to create better or similar grain control effects as other types of continuous magnetic field methods is very attractive for developing green and sustainable metal manufacturing routes.

In the past two decades, extensive research efforts have been conducted on understanding the underlying mechanisms of grain refinement via PMF. For example, Zhai et al. [33], Gong et al. [34] and StJohn et al. [35] reported that, when applying PMF or pulse electric current in a pure Al melt, the grain refinement effect was only found at the grain nucleation stage rather than in the grain growth stage. They argued that this was because the grain nuclei, formed heterogeneously on the relatively cold mould wall, were “shaken” off and moved into the melt by the oscillating force of the PMF. Zhao et al. [36] found that PMF-induced forced convection can homogenize the temperature distribution in the liquid zone ahead of the solidification front. Liotti et al. [37] studied the effect of PMF on the dendrite fragmentation of an Al-15 wt.% Cu. They found that the increase in dendrite fragmentation rate and the grain refinement effect were attributed to the rapid remelting of the most vulnerable microregions induced by PMF. Li et al. [28] proposed that applied PMF could introduce extra energy into the melts, reducing the energy barrier for nucleation and lowering the critical nucleus size, ultimately leading to a higher nucleation rate. Furthermore, Fautrelle et al. [38–41], Pericleous et al. [42] and Ren et al. [25] also studied systematically the solidification dynamics of intermetallic phases in high static magnetic fields. Their research has revealed that thermoelectric magnetic convection (TEMC) becomes a significant mechanism for controlling the growth of intermetallic phases when the magnetic flux intensity exceeds 2T.

In summary, most previous studies have provided valuable insights into the effects of magnetic fields on grain nucleation and refinement in different alloys. However, majority of these studies have focused on the evolution of dendritic structures or intermetallic phases under the influence of high static magnetic fields. The effects of PMF on the nucleation and growth dynamics of intermetallic phases has not been systematically explored. Furthermore, except for a few recent reports by Cai et al. [43–46] and Ren et al. [47], most prior investigations were conducted ex-situ, and the resulting microstructures were assessed post-solidification. Consequently, many interpretations and arguments found in the existing literature regarding the nucleation and growth dynamics of intermetallic phases were based on indirect experimental evidence or hypotheses, lacking real-time, in-situ experimental data. Consequently, the underlying mechanisms are still the subject of intense debate, leading to some conclusions that are either controversial or specific to particular alloys. For example, Mikolajczak et al. [48] suggested that β-Al5FeSi intermetallic phases might undergo fragmentation or remelting due to forced convection induced by magnetic fields. Conversely, Ren et al. [25] contended that magnetic fields might not fracture NiAl dendrites but rather, the TEMC within the interdendritic regions could be responsible for the development of high-order dendrite arms.

In the past ten years or so, researchers in Mi’s group have conducted a series of synchrotron X-ray studies on the microstructural evolution of different alloys under PMF [49–53]. Here, we present the very recent results on the evolution of primary Al_3Ni phases observed in operando using a special PMF solidification device and synchrotron X-ray radiography and tomography at the branchline I13-2 of the Diamond Light Source (DLS), UK. We chose the Al-15 %Ni alloy because the magnetic permeability of the solidified primary Al_3Ni phases is ~3.3 times higher than that of the Al melt. Such difference makes the alloy a perfect model material for us to study the different response of the solid Al_3Ni phases and the melt with respect to the applied magnetic pulses. In addition, the high absorption contrast between the melt and solid Al_3Ni phases gives very high-quality X-ray radiography and tomography data. A multi-physics numerical model was also developed for calculating the magnetic pulse induced Lorentz forces (stresses), fluid velocity field and the differential shear stresses acting on the intermetallic phases and the melt. This work provides systematic data and quantitative understanding into the mechanisms of how the applied magnetic pulses disrupt the growth direction of the primary Al_3Ni intermetallic phases and the critical conditions for phase fragmentation and phase alignment to occur in the PMF. The research establishs a robust theoretical framework for quantitative understanding of the intermetallic phase growth dynamics in solidification under pulse magnetic fields.

2. Methods

2.1. Experimental methods

2.1.1. Alloys and samples

An Al-15%Ni (weight percentage) alloy was used in the experiments and it was made by melting high-purity Al (99.999 %) and Ni (99.99 %) ingots feedstock in an alumina crucible (ID of 92 mm and height of 135 mm, Almath, UK). The crucible was coated with boron nitride spray at its inner surface and then placed inside an electric resistance furnace. It was heated to 900 °C and held at this temperature for ~60 min to gradually dissolve the Ni into the Al melt. Finally, the homogenised alloy melt was drawn uphill under a negative pressure (~0.5 atmospheric pressure) into quartz tubes (100 mm long and 2 mm inner diameter) by using a custom-made counter-gravity casting apparatus. The melt flew quiescently into the quartz tube and solidified as round bars as described in [52]. Fig. S1 shows the Al-Ni binary phase diagram (the Al-15%Ni liquidus is at 782 °C), the X-ray attenuation length for the Al, Ni, Al-15% Ni melt and Al_3Ni phase respectively, as well as the typical as-cast microstructures.

2.1.2. Experimental apparatus and magnetic pulses

Fig. 1 shows the purposely-built PMF solidification apparatus. It consists of (1) two in-house built small electrical resistance furnaces, one stacked on top of the other, (2) a Cu coil wound concentrically outside the two furnaces, and (3) a programmable electrical current pulse generator connected to the Cu coil to produce pulse magnetic fields inside the alloy samples.

Application of the magnetic pulses were synchronized with the X-ray imaging. In this work, we used the peak value of the pulse to represent the magnetic flux density. The pulses were measured in real-time by (1) a 100 MHz bandwidth digital oscilloscope (TENMA, 72-8240) and (2) an axial probe positioned at the centre of the coils (without furnace and samples) and linked with (3) a gauss meter (HIRST Magnetics GM08, UK).

2.1.3. Temperature control during solidification

Fig. 2a shows the measured temperature profiles of the experiments in a series of heating-cooling cycles. The Al-15%Ni alloy samples were heated up above their liquidus temperature (T_{Liq}= 782 °C) and then cooled down near to the eutectic temperature ($T_{Eutectic}$=639.9 °C) and

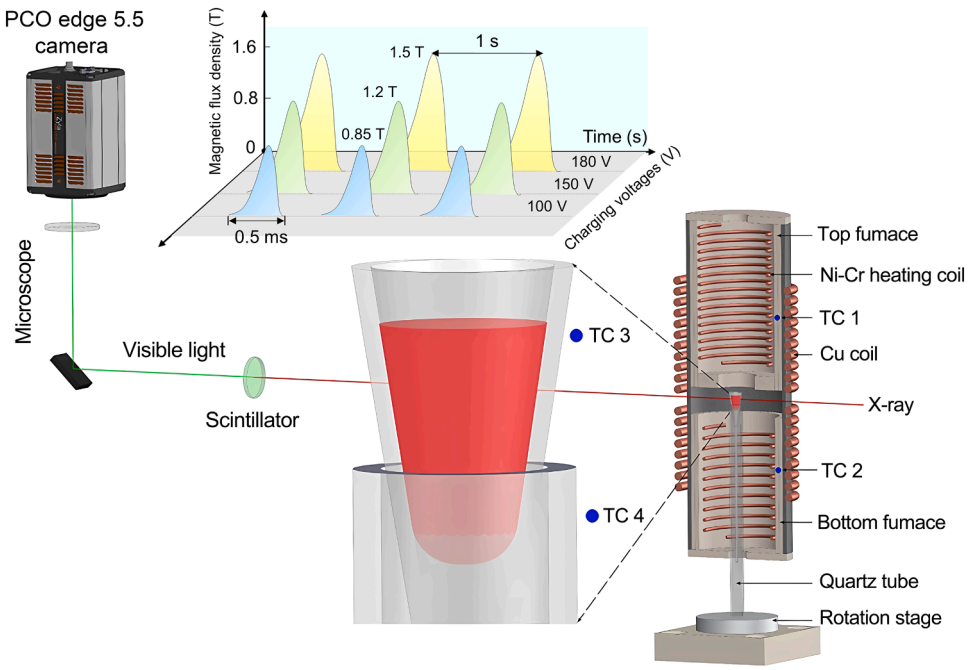

Fig. 1. A CAD rendering of the PMF solidification apparatus and the set up at the I13-2 branchline of DLS. The inset depicts the pulses of magnetic flux densities with their peak in the range of 0.85 - 1.5T (controlled by varying the input voltages [13,52]). The pulse duration is ~0.5 ms and frequency is 1 Hz.

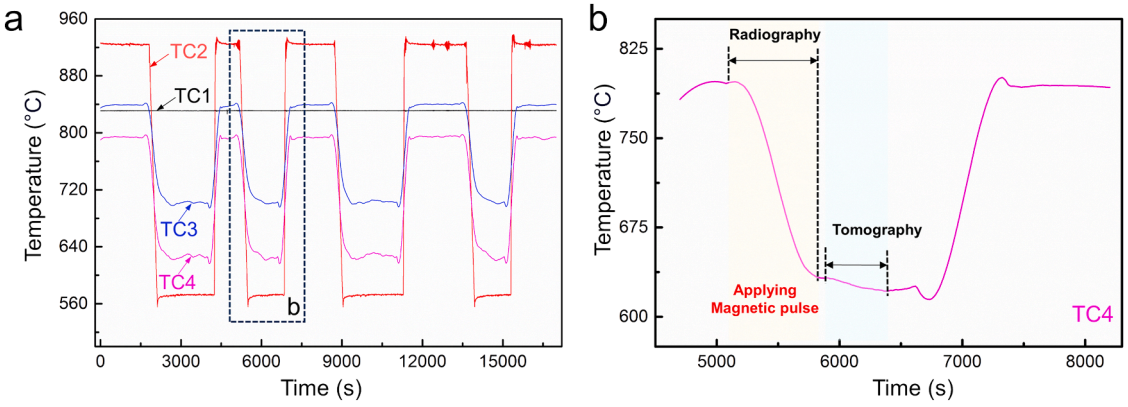

Fig. 2. (a) The measured temperature profiles of the two furnaces at TC1 and TC2; and those close to the alloy sample at TC3 and TC4 in a number of repeated heating-cooling cycles during the operando experiments. (b) The temperature recorded by TC4 in one cycle (the dotted line framed region in a), showing when and how long the PMF was applied, and the start and duration of the radiography and tomography acquisitions.

held there for the Al_3Ni intermetallic phases to grow. We used the built-in program (PLATINUM, Omega, UK) designed for the thermal controller to realise multi-step ramping up/down and soak operations to control precisely the temperatures of the furnaces and the alloy melt during the heating and cooling cycles. The top and bottom furnaces were initially heated to ~835 and ~925 °C to melt the alloy and then held for 60 min to homogenise the temperature of the melt (Fig. 2a). Next, the temperature of the upper furnace was maintained at ~835 °C, the temperature of the bottom furnace was ramped down from 925 to 580 °C in 15 min (an average cooling rate of ~0.35 °C/s) using the control program.

The temperature at TC4 is shown in Fig. 2b, indicating the start of PMF and radiography and tomography acquisitions. Radiographic images were taken continuously until the measured temperatures of the locations (TC 3 and TC 4) reached at 725 and 640 °C (in the semi-solid region) respectively. The TC4 temperature during tomography scan was controlled at ~640 °C, slightly above the eutectic temperature (T_{eut}). Hence no eutectic phases were formed during the tomography scans. The time needed to switch from radiography to tomography was ~60 s. Then, the temperatures of both furnaces were maintained and tomographic images were taken until next cycling. The average cooling rates were 0.35 °C/s (measured at the location TC4). Such heating/cooling operations were repeated for several cycles to ensure different samples were subject to identical thermal conditions. The temperature gradient in the sample was ~2.5 ℃ /mm (see Section 4.2 of the Supplementary Materials).

2.1.4. *Synchrotron X-ray parameters and image processing*

The experiments were carried out at the I13-2 of DLS. A polychromatic X-ray beam was used to illuminate the samples. It was generated by an undulator of 5 mm gap and was reflected from the platinum stripe of a grazing-incidence focusing mirror and high-pass filtered with 1.3 mm pyrolytic graphite, 3.2 mm aluminium and 20 μm steel. Images were recorded by a CMOS (2560×2160 pixels) pcoedge 5.5 camera (PCO AG, Germany) which was coupled to a 500 μm-thick CdWO4 scintillator and an optical microscope. 4 x objective lens was

used, achieving 0.81 μm/pixel effective spatial resolution in a field of view (FoV) of 2.1×1.8 mm. 0.1 s exposure time was used to achieve a sufficient signal-noise ratio. In the tomography experiments, a total of 2001 equally-spaced projection images were acquired over 180 degrees continuous rotation for each sample. The radiographic images, darkfield and flat field images were normalized using Fiji. Tomographic reconstruction was performed at DLS using the in-house software SAVU [54, 55]. The 3D median filter with 1-pixel radius was used to reduce the noise of those images before segmentation.

For the radiographic images, we used the Trainable Weka Segmentation plugin [56,57] in Fiji to distinguish the Al_3Ni phases from the melt based on the grayscale criterion set for the Al_3Ni phases. The plugin combines numerous machine learning algorithms for defining and then selecting a set of specific image features in order to enable pixel-based segmentations. To ensure accurate detection and identification of the features, a classifier that meets the criterion has to be obtained through multiple training sessions. After segmentation, we employed the Analyze Particles built-in plugins to measure the area and length of each Al_3Ni phases [57]. For tomography data, we used Avizo software for visualization and quantitative analysis. We applied the watershed segmentation algorithm [58] to segment and identify the Al_3Ni phases. The number of the Al_3Ni phases and the volume of each phase were determined using a labelling algorithm and line probe within the Avizo module called Label Analysis. In addition, we also used the skeletonization function and the separate objects algorithm in Avizo to calculate the length, surface area, volume and phase orientation (from 0 to 90°) of each Al_3Ni phase.

3. Results

3.1. Al_3Ni phase growth and branching dynamics

Fig. 3 and Video 1 show the growth dynamics of the primary Al_3Ni phases under magnetic flux densities of 0, 0.85 and 1.5 T respectively. In the 0 T case, Fig. 3a1 shows that a few Al_3Ni phases first appeared in the FoV. 1 large phase seemed to fall into the FoV from above, floating freely in the liquid, rotating ~60° clockwise in 0.3 s and then reaching the location shown in Fig. 3a2. Clearly it was driven by the density difference between the Al_3Ni phase (3.817g/cm^3) and the liquid melt (3.014 g/cm^3). Fig. 3a3 shows many randomly orientated Al_3Ni phases appeared in the FoV after 16 s, and they continued to grow and coarsen (Fig.3a4). In the 0.85 T case, the Al_3Ni phases appeared firstly at bottom of the FoV (Fig. 3b1). Majority of the subsequently nucleated Al_3Ni phases grew along the directions pointed out by the black arrow in Fig. 3b2. At later stage of growth (Fig. 3b4), some phases seemed to cross over others and frequent phase branching occurred. In the 1.5 T case, the

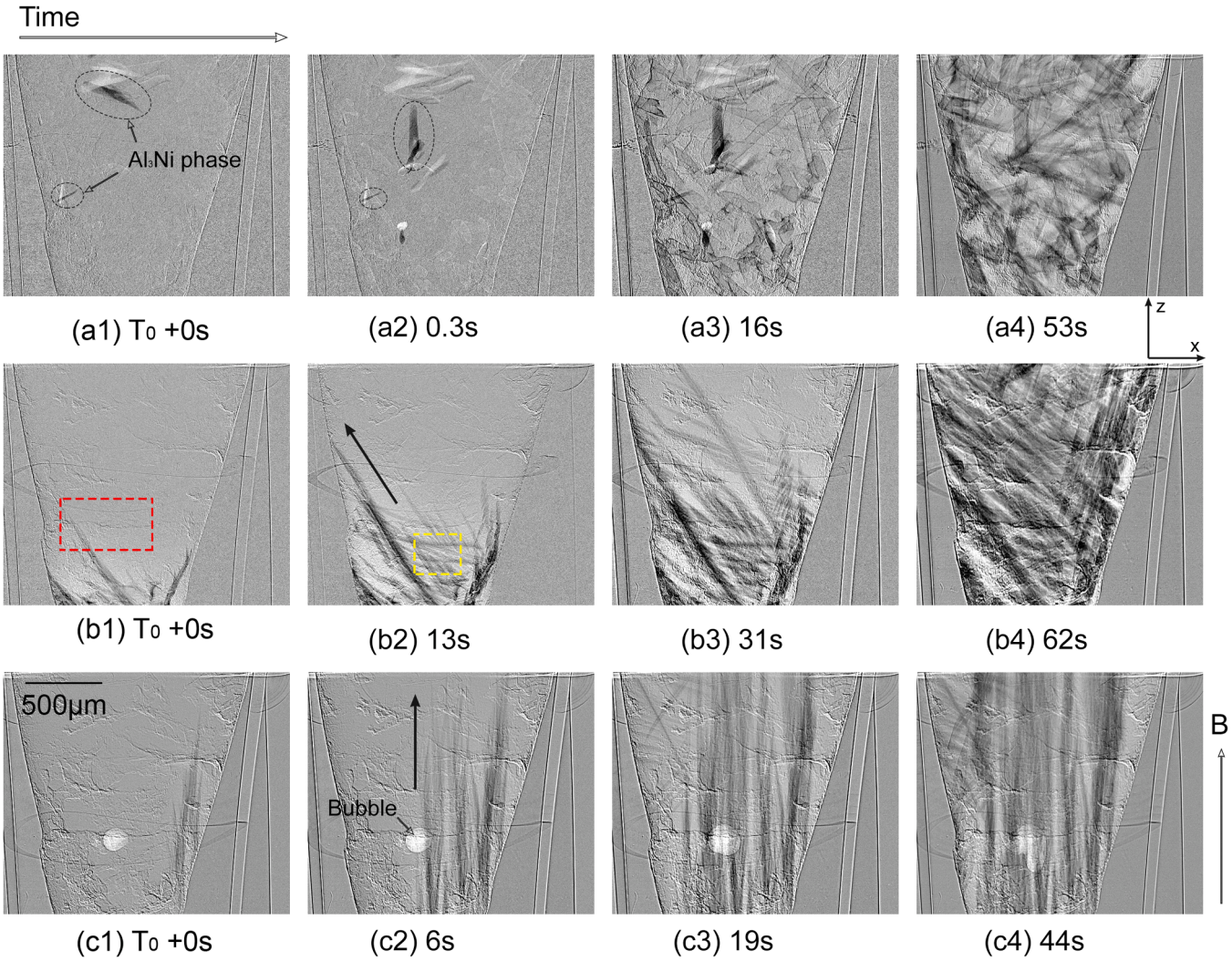

Fig. 3. Three rows of synchrotron X-ray radiographs, showing the growth dynamics of primary Al_3Ni phases (the black phases) in the Al–15 %Ni melt (the grey matrix) during solidification with peak PMF flux density of (a) 0 T, (b) 0.85 T, and (c) 1.5 T, respectively. The cooling rate is V = 0.35 °C/s. The 500 μm scale bar is for all images. Video 1 shows more vivdly the growth dynamics of the Al_3Ni phases in the three cases.

first few Al_3Ni were seen on the right-hand side (Fig. 3c1), growing vertically and aligned in parallel with the magnetic flux direction (see the arrow in Fig. 3c2). Subsequently, more Al_3Ni phases continued to grow from the right to the left in the FoV (Fig. 3c2-4) and maintained their vertical growth direction. Also, in the left upper part, the growth direction of a few Al_3Ni phases seemed to not change much (see Fig. 3c3-c4), i.e., the applied pulse had little effect on their orientation. This was because in the late stage of solidification, the solid volume fraction was much higher and there was not enough free space in the remaining liquid for the phases to move or realign.

Fig. 4 and Video 2 show the Al_3Ni phase branching dynamics in the case of 0.85T case. The Al_3Ni phases grew into the red rectangular area in Fig. 3b1 were enlarged and shown in Fig. 4a. First, the primary trunk grew into the FoV (Fig. 4a1). In next few seconds, side branches appeared and grew laterally (Fig. 4a2). Finally, a few tertiary branches parallel to the primary trunk appeared and gradually occupied the whole FoV (Fig. 4a3 & a4). From Video 2, we extracted one typical Al_3Ni phase to show the instance when the side branches and tertiary branches started. The processed and rendered Al_3Ni phase are shown in the top part of Fig. 4c. The morphology of the primary trunk and its spatial correlation with the side branches and tertiary branches are clearly illustrated. The tip growth velocities of the primary trunk, side and tertiary branches were measured from the X-ray images and shown in Fig. 4b and c. In the 0 T case, there were no side and tertiary branching, and the average growth velocity of the primary trunk was 50±25 μm/s. In the 0.85 T case, the primary trunk and the side branches started to grow along the preferred direction with the growth velocity in the range of 160±80 μm/s. In the 1.5 T case, majority of the Al_3Ni phases grew along the magnetic flux direction with the growth velocity of ~425 μm/s (Fig. 4b).

3.2. Al_3Ni phase fragmentation

Fig. 5 and Video 3 show the Al_3Ni phase fragmentation behaviours in the case of 0.85T. The Al_3Ni phases fragmentation events at the yellow rectangular area in Fig. 3b2 were enlarged and shown in Fig. 5a. Two typical regions in Fig.5a were zoomed in again (Fig. 5b and c) to illustrate more clearly the downwards movement of two phase fragments (marked in red) occurred in the inter-dendritic region between the larger phases (in ms time scale). In Fig. 5d, the total number of the detached Al_3Ni phases in the whole FOV was counted and plotted against time. Additionally, Fig. 5e depicts the number of the detached Al_3Ni phases in the two rectangular regions (b & c) of Fig. 5a. Clearly, most phase fragmentation and detachment occurred in the first 5-6 s. Video 3 demonstrates more clearly the falling movement of the broken off fragments.

3.3. Al_3Ni phase 3D morphology and orientation

Although the time-resolved radiography images provided rich dynamic information about the growth of the Al_3Ni phases, the overlapping nature of the 2D projections (Fig. 3) makes it very difficult to differentiate each individual phase. Hence, tomography data were acquired when the melt temperature was maintained at ~640 °C (i.e., above the eutectic temperature) for each case after radiography acquisition. Fig. 6 shows the segmented and rendered Al_3Ni phases in 3D (the remaining liquid melt were removed).

A few typical phases were extracted from the whole tomography data and shown on the right for each case. In the 0 T case, the Al_3Ni phases have random orientation with long and blocky morphology (Fig. 6b & d). In the 0.85 T case, phases with more side branches started to form (Fig. 6f & h). At 1.5 T, majority of the Al_3Ni phases grew into dendritic morphology with well-developed secondary and tertiary branches (see Fig. 6j & l). From the tomography data, we also extracted the orientation (from 0 to 90°) and length distribution information of the Al_3Ni phases. As shown in Fig. 6m for the 0 T case, >55 % of the phases were <1 mm and the maximum length was ~1.9 mm. However, in the two PMF cases, in the similar solidification time, the phases were approximately twice longer than those in the 0 T case. The longest phases were ~2.7 mm which were the curved Al_3Ni phases resolved in the tomography. Fig. 6n shows the phase orientation distributions. The phase orientation angle is the angle between the central line of a phase in the length direction and the horizontal X-axis. In the 0 T case, the phases are randomly orientated. While, at 1.5 T case, approximately 60 % Al_3Ni phases were aligned over 70 ° and 75 % are over 50°. Obviously, the peaks shift from an angle of 35 to 70° when the magnetic flux density increased from 0 to 1.5 T, indicating that the PMF plays a crucial role in rotating and

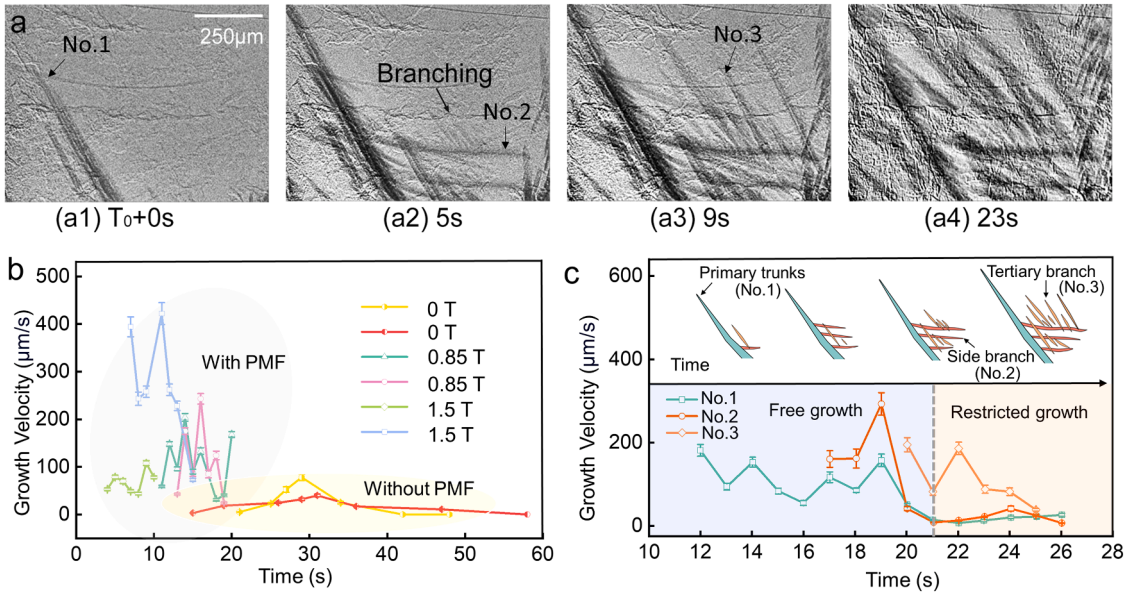

Fig. 4. (a) The Al_3Ni phases branching dynamics (images taken from the red rectangle area in Fig. 3b1); (b) the tip growth velocities of the primary trunks in the case of 0, 0.85 and 1.5 T respectively; (c) the tip growth velocity of the primary trunk, side branches and tertiary branches in the 0.85 T case. The rendered Al_3Ni phases shown in the top half of (c) are the phases marked by No.1~3 in (a). The dotted vertical grey line in the lower half of (c) marks the transition between different growth modes: (i) the free growth on the left-hand side where the Al_3Ni phases grew freely in the melt; (ii) the restricted growth on the right-hand side because the Al_3Ni phases' growth were affected by the nearby phases or the quartz tube wall. Video 2 illustrates more clearly the branching dynamics of the Al_3Ni phases.

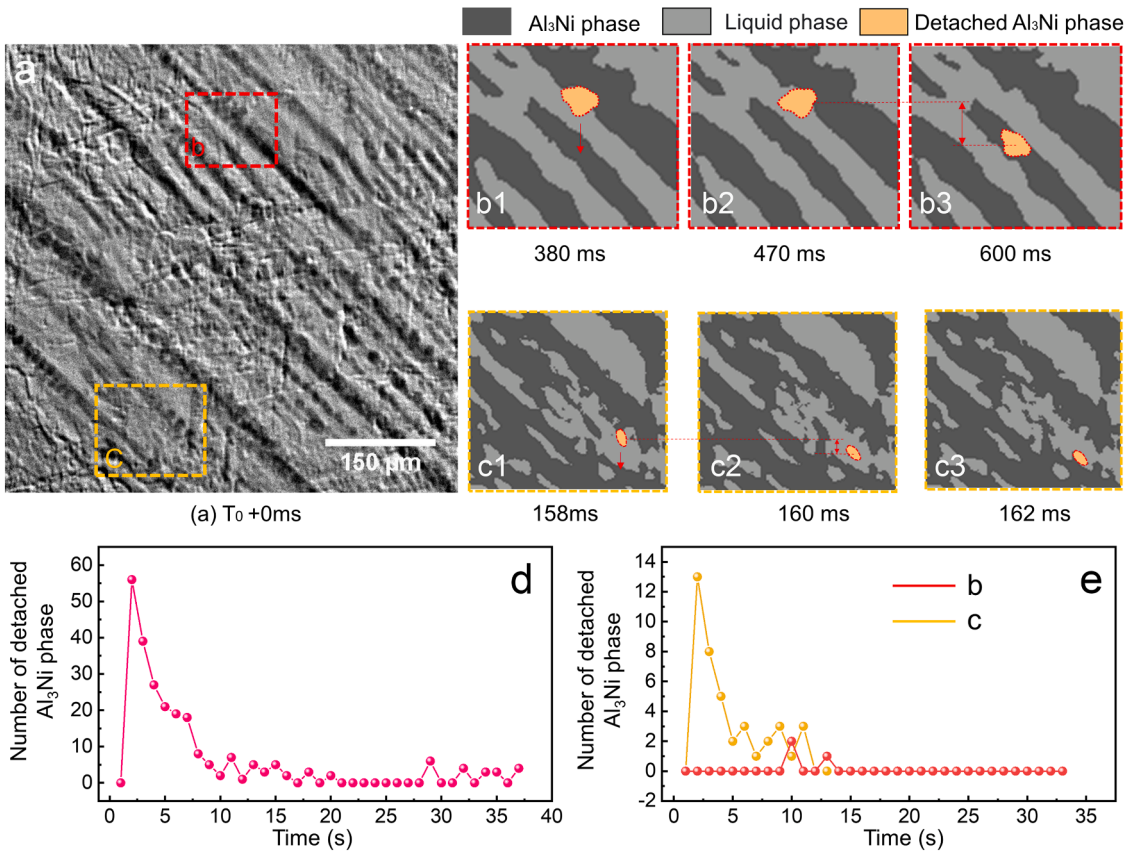

Fig. 5. (a) A typical X-ray image, showing the Al_3Ni fragmentation events under 0.85 T, (b) and (c) the red and yellow rectangular areas in (a) are extracted and enlarged, showing smaller Al_3Ni fragments broken away from the larger growing Al_3Ni phases. (d) and (e) show the number of detached phases over time in the whole FOV in (a) and in the two rectangular regions (b & c) in (a), respectively. See Video 3 for the falling down movement of the broken off Al_3Ni fragments.

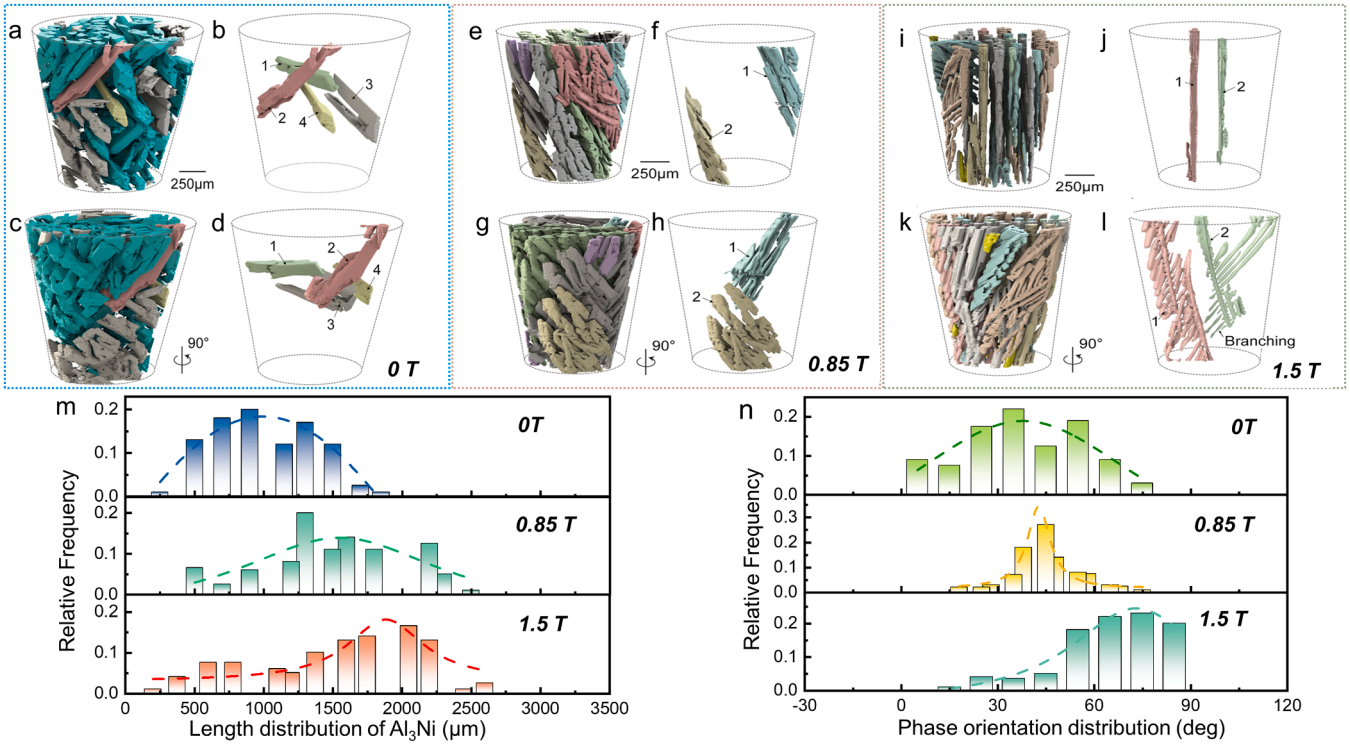

Fig. 6. Tomography of the Al_3Ni phases above the eutectic temperature with peak PMF flux density of 0 T (a-d), 0.85 T (e-h) and 1.5 T (i-l), respectively. (m) and (n) show the length and orientation distribution of the Al_3Ni phase, respectively. See Videos 4~6 for appreciating the true 3D morphology of these Al_3Ni phases when viewing from different angles, espically the dendritic Al_3Ni phases in the 1.5 T case.

reorienting the Al_3Ni phases (towards to the flux direction).

3.4. Multiphysics modelling

To understand more quantitatively the effects of PMF on the growing phases in the solidifying melt cross multi-time scales, we developed a Multiphysics model using the same geometry domain as the experiment. Fig. 7a shows the computational domain, the mesh structure and boundary conditions. A real Al_3Ni phase extracted from the tomography datasets (i.e., the Al_3Ni marked by 2 in Fig. 6l) was used in the simulation as shown in Fig. 7b. The multiphysics account for in the model are (1) non-linear heat transfer with calculation of the latent heat release in solidification, (2) natural convection driven by gravity and forced convection (fluid flow) induced by PMF, (3) electric current pulse induced magnetic pulse, (4) induced Lorentz forces and stresses by the PMF. The governing equations, numerical methods and thermophysical properties used in the simulation are described in Section 2 of the Supplementary Materials.

3.4.1. Magnetic field and model validation

To validate the numerical model, the results from the modelling and experiments were compared at the same conditions. The calculated and measured magnetic pulse profiles in Fig. 7d & e matched very well. For instance, when the applied voltage was 180V, the peak magnetic intensity at the centre of the trapezoidal sample is calculated as ~1.5T. We also tracked the magnetic field profile over time along line1 & 2 in Fig. 7c. When the pulse was just triggered, the magnetic field intensity in the middle of the sample is weaker than on either side, but it reached its maximum in 0.25 ms. We then focused on studying the Lorentz forces and the resulting stresses produced by the PMF on the Al_3Ni phases and the nearby melt.

3.4.2. The Lorentz forces and stresses

Fig. 8a-c show the vectors of the Lorentz forces per square meter induced by PMF in the Al_3Ni phases at 0.1, 0.2 and 0.4 ms in a single pulse period. The Lorentz force on the tip of the side branch was 6.2×10^3 (N/m^2), much higher than the force at the primary trunks. We selected 5 typical locations (P1~P5) on the Al_3Ni phase in Fig. 8d, representing the typical geometrical characteristics of the Al_3Ni phase. Fig. 8e-g show the radial Lorentz forces acting on the solid Al_3Ni phases and the nearby melt. In one pulse period of ~0.5 ms, The Lorentz forces at all locations exhibited like a sine wave, starting with negative (compressive forces), then changing to positive (tensile forces), and finally damping out at ~0.52 ms. Such force direction change was due to the direction change of the induced current in the solid phase produced by the applied PMF. In one pulse period, the 1st half period is a rapid ramping up of the flux,

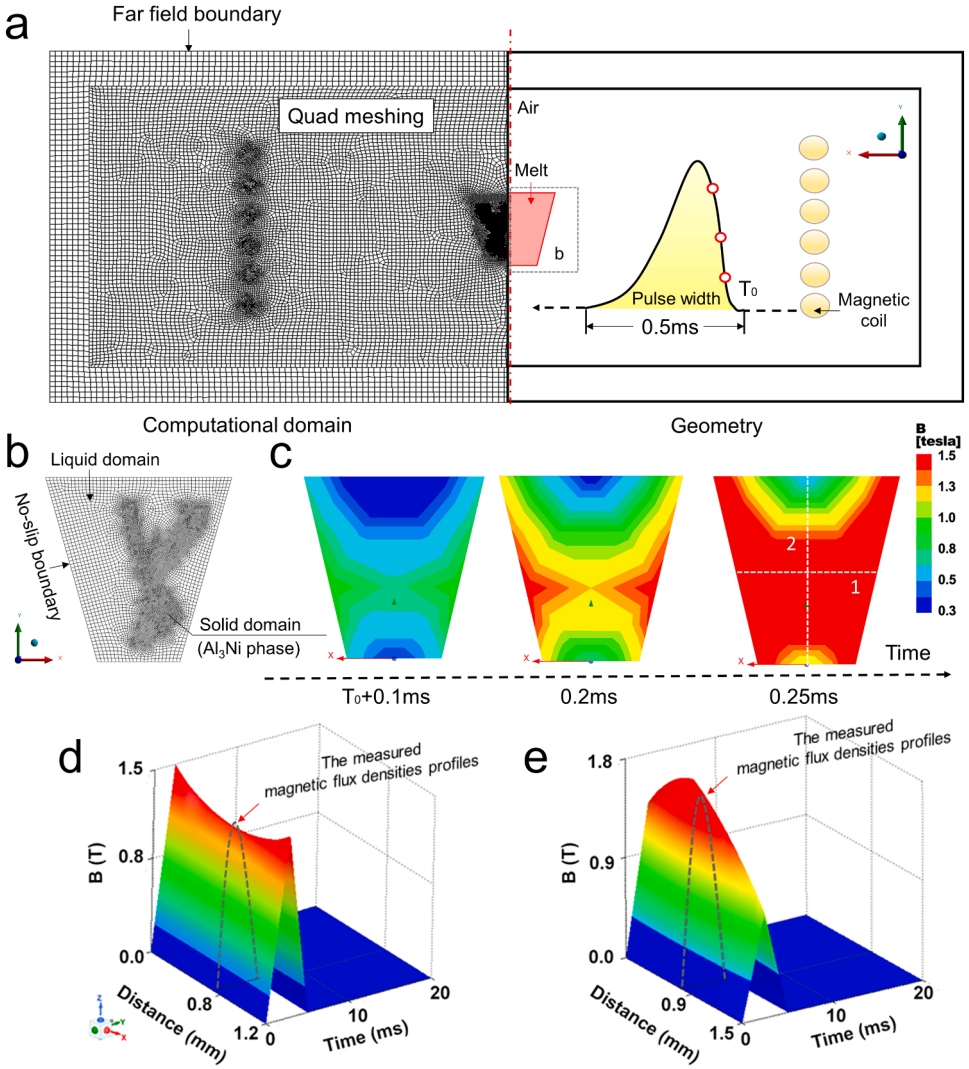

Fig. 7. (a) The computational domain and (b) mesh structures for the domain (quad meshes) and the Al_3Ni sample (unstructured meshes). (c) The magnetic field contour with peak flux density of 1.5 T in a single pulse period at 0.1, 0.2, and 0.25 ms. (d) and (e) show the magnetic field profiles plotted versus distance and time along line 1 and 2 marked in (c), respectively.

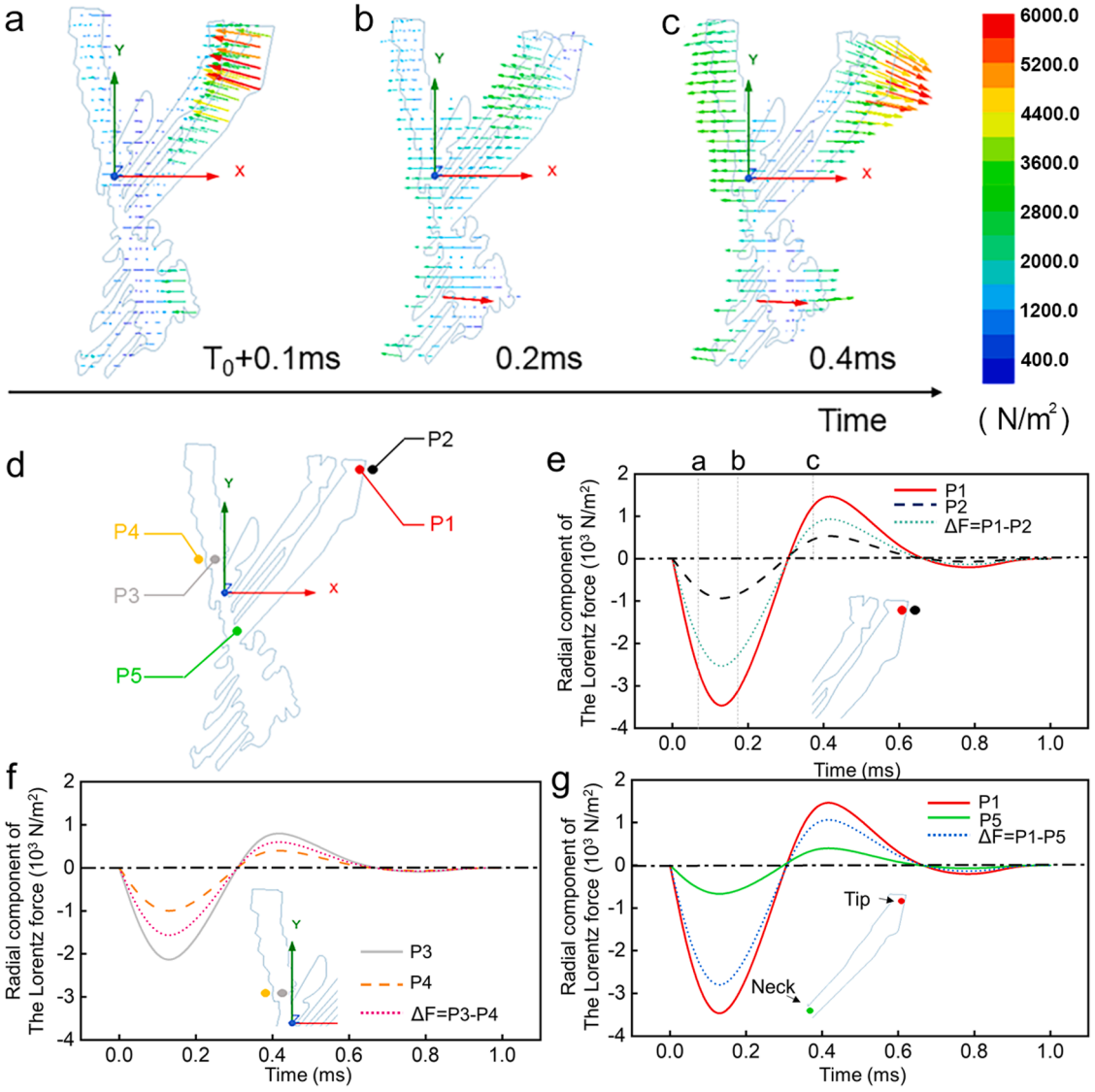

Fig. 8. The Lorentz forces acting on the Al_3Ni phases simulated for the 1.5 T case in a single pulse period at (a) 0.1 ms, (b) 0.2 ms, and (c) 0.4 ms. The calculated radial component of the Lorentz force at (e) P1 (tip of the side branch) and P2 (the melt next to P1). (f) P3 (the primary trunk) and P4 (the melt next to P3). (g) P5 (neck of the side branch).

and then in the 2nd half period, a rapid ramping down of the flux. According to Maxwell's equations, the induced current change direction from the 1st half to the 2nd half period, resulting in the change direction of the Lorentz forces [59]. Moreover, the duration of the compressive force is longer than that of the tensile force. The solid Al_3Ni phases are subject to larger Lorentz force compared to the nearby liquid phase.

The force difference between the side branch and the nearby fluid is much larger than that of the primary trunk and the nearby fluid. This is because the secondary branches grew laterally and close to the magnetic coil, resulting in a stronger Lorentz force received. More importantly, the periodical change of force direction imposed fatigue effect on the solid phase at the solidification front which is the key driving force for the side branching as discussed later.

Fig. 9a~c show the time-evolved stress contour on the Al_3Ni phase in one pulse period. The surface of the primary trunk and side branches near the magnetic coil were subject to higher stresses due to the skin effect of the PMF (Fig. 9d). Similarly, the necks of the side branches were also subject to bending stress as shown in Fig. 9e. To understand quantitatively the fatigue effect on Al_3Ni phase due to the impulsive stresses, we plotted the fatigue stress – life relationship (the S –N curve) for the Al_3Ni phase using the equations below:

$$N = CS^{-\psi} \tag{1}$$

$$lgN = lgC - \psi lgS \tag{2}$$

Where S is the fatigue stress, N is the number of cycles to failure, C and ψ are the material constants. We used the very rich fatigue datasets obtained from the Aligned Al-Al_3Ni Eutectic Alloy to establish the S – N relationship [60]. According to Eqs. (1) and (2), the values of lgC and ψ were obtained by a bilinear fitting of lgS and lgN (see Supplementary Materials). Fig. 9f shows the referenced data and the fitted S – N curves in different temperatures, expressed in the number of pulse cycles. Fig. 9g shows clearly that the neck of the side branch experienced a stress of 200 MPa. Hence it fractured in a single pulse period. While for the region subject to 120 MPa, 30 pulses were needed to fracture that region as pointed by the arrow in Fig. 9g.

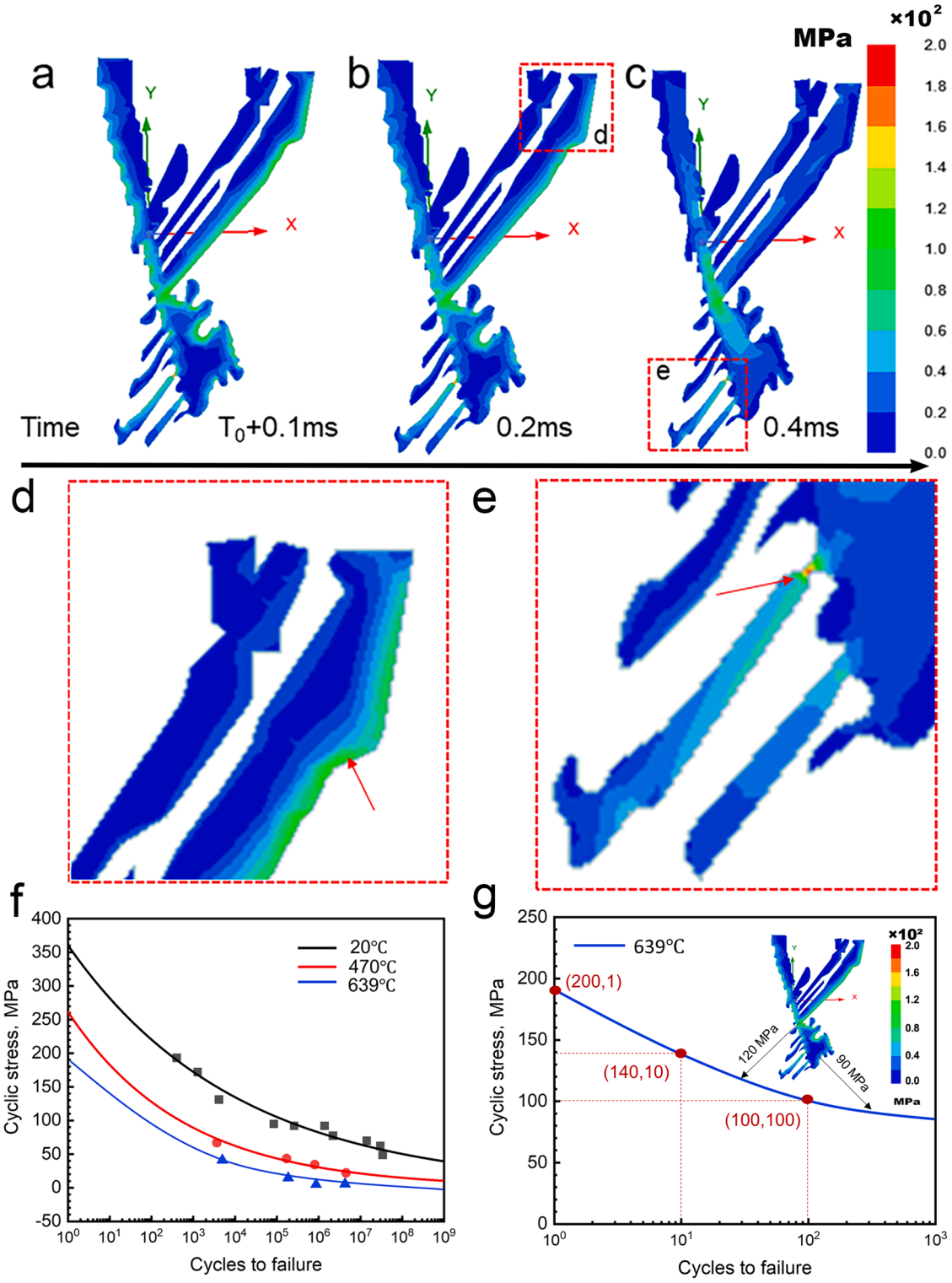

Fig. 9. (a)-(c) The time-evolved stress contour on the Al_3Ni phase produced by the PMF with peak flux density of 1.5 T. Highlighting the stress distribution in the edge and neck regions of the side branches shown in (d) and (e), respectively. (f) the S-N curves of the Al_3Ni dendrite at 20 ℃, 470 ℃ and 639 ℃, the inserted data at 20 ℃, 470 ℃ were referenced from [60] and the data at 639 ℃ were from the Supplementary Materials. (g) the S-N curves of the Al_3Ni dendrite at 639 ℃ in the range of 1-1000 cycles.

3.4.3. PMF induced forced convection surround the Al_3Ni phases

In addition to the Lorentz forces (stresses), the PMF also produced forced convection in the melt as shown by the velocity contour maps in Fig. 10d, e and f for the three cases (i.e., 0 T, 0.85T and 1.5T). Three typical points (P6, P7 and P8 in Fig. 10a, b and c respectively) were chosen to illustrate the typical locations at the front of the liquid-solid interface for the primary trunk (Note the solute boundary layer in each case is highlighted with reddish colour, but this is just for visualization purpose, it is not the actual solute boundary layer). At P6 (i.e., 0 T), the flow velocity was 0.4~0.5 mm/s. However, at P7 (i.e., 0.85 T) when the pulse arrived, the flow velocity rapidly ramped up and reached a peak value of 2.3~2.7 mm/s and then it ramped down with the similar

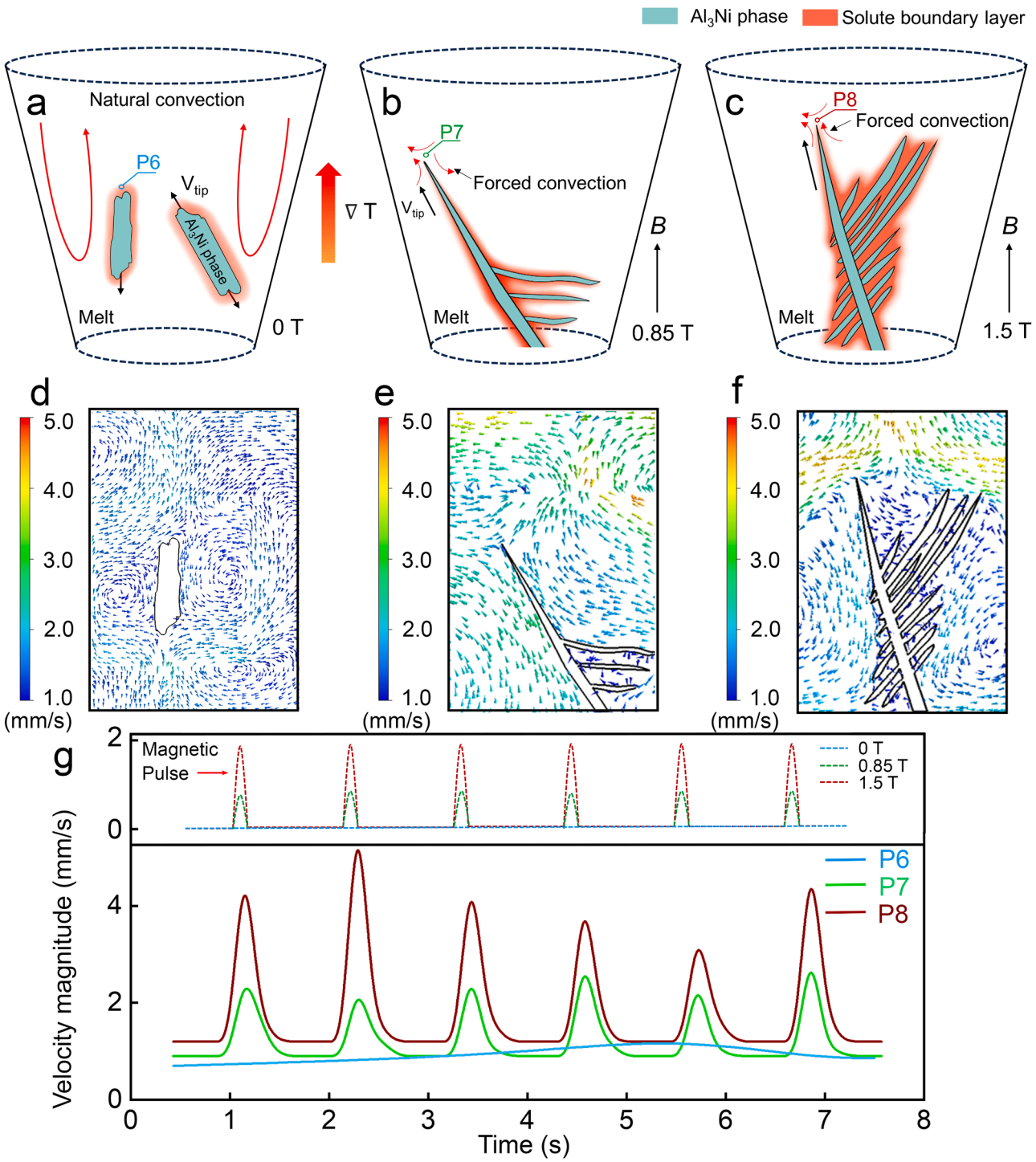

Fig. 10. (a) (b) and (c) are the typical Al_3Ni phases selected from the radiography videos for the case of 0 T, 0.85 T and 1.5 T respectively, illustrating the morphology at the chosen time step during growth. P6, P7 and P8 indicate the typical locations at the immediate front of the liquid-solid interface for the Al_3Ni phases. (d), (e) and (f) are the simulated velocity vector maps for the three cases at the instance of when the peak magnetic flux is arrived; (g) the simulated fluid flow velocity profiles at P6, P7 and P8 respectively in one pulse period. Note: the solute boundary layer rendered by the reddish colour are just for visualisation purpose. It is not the actual boundary layers.

rate. At P8 (i.e., 1.5 T), the peak velocity reached 4.5~5.4 mm/s (Fig. 10g). Due to the inherent inertia and viscous dissipation effect of the melts. The velocity exhibited the similar pulse profile as the magnetic pulse, but with much longer duration, typically in ~0.5 s, approximately 1000 times longer than the duration of the magnetic pulse (i.e., 0.5 ms). Also, the velocity profiles followed the same frequency as the input magnetic pulses, i.e., at 1 Hz.

4. Discussion

4.1. Phase growth dynamics under PMF

A few studies including experiments have been conducted to investigate the intermetallic growth dynamics [46,47,61]. Here, the systematically acquired radiography and tomography data allow us to track

precisely the time-evolved intermetallic growth, branching and fragmentation dynamics. Firstly, the Al_3Ni tip growth velocities were substantially increased by the PMF. At 0.85 T, the growth velocity was in the range of 80 ~ 240 μm/s and the average velocity was much higher than the case of 0 T (<100 μm/s). At 1.5 T, the peak growth velocity reached ~425 μm/s (see Fig. 4b).

Al_3Ni is solute-rich phase with solute distribution coefficient, $k > 1$. Any Al_3Ni crystal growth is accompanied by solute redistribution within the melt, resulting in solute deficiency ahead of the solid-liquid interface that may slow down any further growth. The melt velocities in Fig. 10 d, e. f and g indicate that, at the tip of the Al_3Ni phase, the flow velocities were 0.4~1.2 mm/s for 0 T, 1.8~2.4 mm/s for 0.85 T, and 3.5~4.9 mm/s for 1.5T, respectively. Hence the enhanced melt velocity is 4-8 times higher compared the 1.5 T with the 0 T case. Although the velocity exhibited the similar pulse profile as the magnetic pulse, it lasted much longer (~0.5 s, ~1000 times longer than the duration of the magnetic pulse). Undoubtedly, such enhanced forced convection is able to accelerate the mass transport near the tip of the Al_3Ni phase, bringing in more solute atoms to the interface front and therefore increase the growth rate of the Al_3Ni phases. Fig. 4b and c show that the measured tip growth velocities oscillated to a certain degree. This again can be linked to the pulsed melt velocity profile shown in Fig. 10g, which is active for only 0.5 ms in one magnetic pulse cycle (1 s), causing oscillated growth profiles.

4.2. New mechanism of phase branching under PMF

Secondly, most previous studies found that the instability induced by external fields plays a key role in phase branching. For example, Li et al. [62] proposed that the instability of cells and dendrites in a high magnetic field was attributed to the thermoelectric magnetic force (TEMF) in the solid dendrite and cell. In our work, the 2D radiographs clearly show the morphology changes of the Al_3Ni phases from the facet growth to dendritic growth as the pulse flux increased (see Fig. 3). Furthermore, Fig. 6 illustrates clearly the 3D morphology of the secondary and tertiary branches. For the Al_3Ni phases (crystals), the [001] and [010] crystal directions are the easy magnetic axis and the loose-packed crystal planes. The (011) and (01$\bar{1}$) planes are closely packed crystal planes. According to the classical crystal growth theory, the ability of liquid atoms attachment onto a solid surface varies with the atomic density and crystalline interplanar spacing. It is easier for liquid atoms to adhere onto the loosely packed crystal planes than onto the close-packed crystal planes. Hence, under an identical condition during phase growth, the [001] direction is the preferred growth direction for the Al_3Ni phases [38]. Fig. 8e shows that the peak Lorentz force at the tip of the Al_3Ni phase is approximately 3.5 times higher than that at the adjacent melt, producing a shear force acting on the growing crystal front. Fig. 11a illustrates schematically a mechanism of how such shear force can cause a slip dislocation in the growing crystal front. Under the repeated actions of the applied pulses, such slip dislocation may develop further into nm and then μm scale crystal steps. Many evidences were found in the 2D radiography and 3D tomography for such μm scale steps. One typical example is highlighted in Fig.11b.

In previous studies, Lan et al. [63,64] demonstrated that an external flow field can promote phase side branching using adaptive phase simulation, but its flow velocity is approximately Centimeters per Second level, which is much larger than the forced convection caused by PMF. Fig. 11c & d show the Al_3Ni phases branching dynamics in the 0.85 T case and the final 3D morphology. The primary trunk of the Al_3Ni intermetallic phase was observed to initially grow in a direction offset by 45° from the vertical axis. Subsequently, under the PMF, secondary side branches appeared in the horizontal direction. This confirms our argument that the initiation of side branches started with the creation of the slip dislocation.

4.3. New mechanism of phase fragmentation under PMF

Several studies have been conducted to investigate the grain refinement mechanisms in the presence of PMF [28,35,65–67]. The widely accepted theory is that PMF causes more nucleation in the early

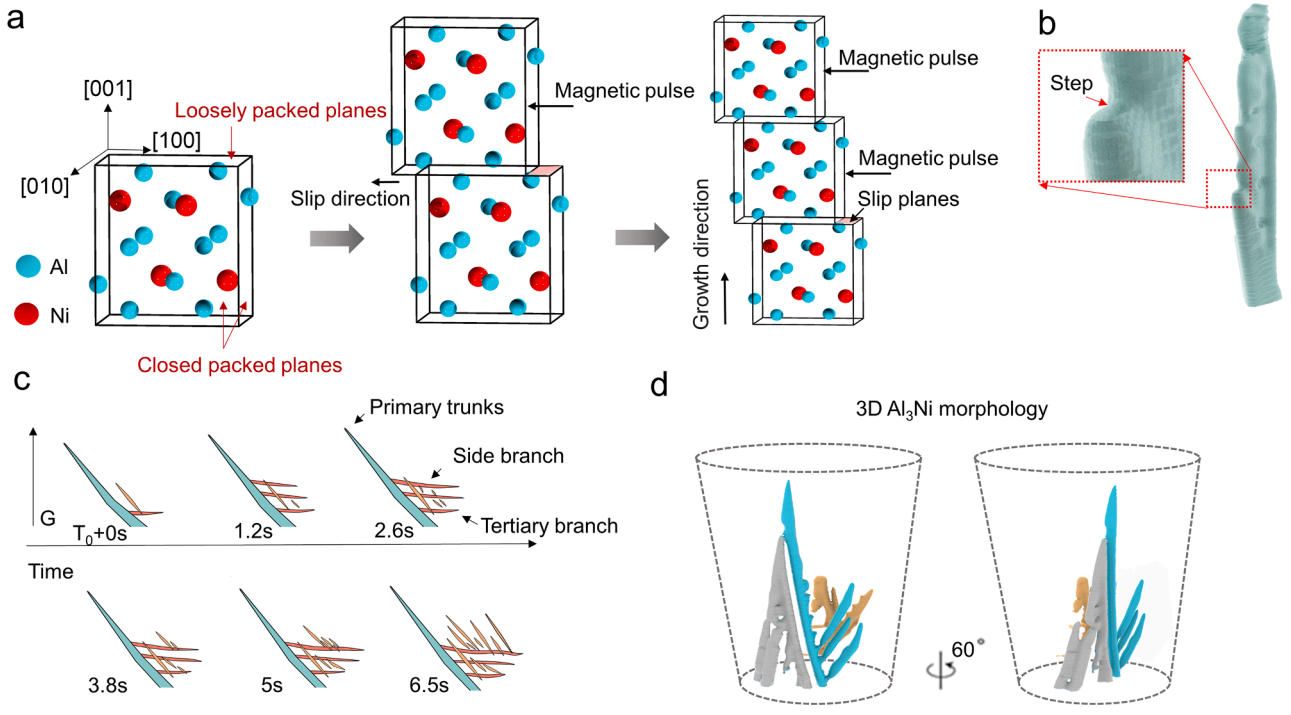

Fig. 11. (a) Schematic illustration, showing the creation of slip-dislocation in growing Al_3Ni crystals under the PMF. (b) A typical Al_3Ni phase with numerous micro-steps extracted from the tomography data. (c) The Al_3Ni phases branches growing out of from these micro-steps in the case of 0.85 T. (The extracted images were from Video 1 and Video 2). (d) The final 3D morphology of the Al_3Ni phases showed in (c).

stages of solidification [67]. Previous experiment and simulation result suggested that the applied pulses could detach many grains from the mold wall, propelling them towards the center of the melt and resulting in more nucleation [35]. Moreover, based on classical nucleation theory, Zhao and Liu et al. [36] indicated that the magnetic field could provide an additional driving force to the formation of grain nuclei. Therefore, the nucleation rate increases under PMF. Our in-situ observation clearly showed that the Al_3Ni phase fragmentation events occurred in the entire FOV as shown in Video 3. In contrast, no visible fragmentation events were observed in the case of no magnetic field (see Fig. 3a). Our simulation also quantified the forces acting on the different points of the solid phases, those on the nearby locations inside the melt, and the difference between them. In Fig. 9d & e, the stresses acting on the Al_3Ni phase were as high as ~200 and 120 MPa at the side branch necks and near the trunk surface, respectively, which are much higher than the stresses experienced elsewhere (~40 MPa). Furthermore, Fig. 9g also clearly illustrates that, at a given stress level, phase fragmentation occurred when the number of pulse cycles exceed its fatigue life. For example, for the region that experienced a stress of 200 MPa (at side branch necks). It fractured in one pulse. While for the region with ~120 MPa (at trunk surface), it broken off (fragmentation) after 30 pulses.

Fig. 3a and Video1 show very clearly that, without PMF, the solidified bulky Al_3Ni phase rotated and sank downwards under gravity (due to the density difference between the solid phase and the melt). However, no fragmentation or remelting events were observed. We have done three samples without the application of PMF (i.e., under the effect of gravity only). In all three cases, we did not observe any fragmentation events in the radiography videos. Hence gravity is not a major factor in fragmentation.

For the forced convection, simulation results show that the flow velocity induced by the PMF around the Al_3Ni phase ranges from 1.5~5.2 mm/s for 1.5T as shown in Fig. 10f & g. Hence, the bending stresses acting on the surface of the Al_3Ni phase induced by the forced convection is extremely low. By comparison, Fig. 8 shows the Lorentz force (up to 4.8×10^3 N/m^2) acting on the solid phase is three times higher than that on the surrounding liquid phase (1.5×10^3 N/m^2). More importantly, the stresses acting on the trunk surface and side branch necks of the Al_3Ni phases are much higher than elsewhere (see Fig. 9d & e). The higher stressed regions correspond to the locations where phase fragmentation occurred in the X-ray images. All experimental and simulation evidence indicated that the PMF induced stresses are the dominant mechanisms for intermetallic phase fragmentation to occur instantaneously or via a fatigue mechanism. While the induced forced convections are very weak and not able to cause any phase fragmentation.

After a certain amount of Al_3Ni phases were formed in the Al-15 %Ni melt, the Ni concentration in the remaining Al-Ni melt is less than the 25 % atomic percentage needed for the Al_3Ni phases (See Fig. S1 a). In this case, there is no constitutional undercooling at the front of the Al_3Ni solid-liquid interface [68,69]. Therefore, any constitutional undercooling induced phase remelting phenomenon does not exist in the Al-15%Ni alloy. Hence for phase fragmentation, the pulse stresses induced fragmentation is the dominant cause.

5. Conclusion

We used synchrotron X-ray radiography and tomography to study, in operando conditions, the growth dynamics of the primary Al_3Ni intermetallic phases in an Al-15%Ni alloy under pulse electromagnetic fields. A multiphysics modelling was also developed to calculate the differential forces/stresses acting on the Al_3Ni phases, the melt and the forced convections inside the melt. The systematic operando experiments and modelling work allow us to establish a robust theoretical framework for quantitative understanding of the intermetallic phase growth dynamics in solidification under pulse magnetic fields. The important new findings of this research are:

1. The magnetic pulses can produce significant differential forces or stresses acting on the Al_3Ni phases and the nearby melt, producing slip dislocations at the growing crystal boundaries and this is the primary driving force for the phase branching to occur.
2. The growing velocity of the Al_3Ni phases and their orientations are greatly affected by the increase of peak magnetic flux density. This is due to the enhanced forced convection induced by the magnetic pulses at the front of the liquid-solid interface, resulted in a much increased growth rate with the increase of magnetic flux density, forcing the Al_3Ni phases to grow into full dendritic structures at the peak flux of 1.5 T.
3. The magnetic pulse induced stresses behave alternatively (from compressive to tensile) and impose on the growing Al_3Ni cyclically according to the applied pulse frequency. Dependent on the morphology and geometrical characteristics of the growing phases, shear stresses of up to 200 MPa can be produced at the narrow neck regions, sufficiently enough to cause fragmentation of the Al_3Ni phases in a single pulse period. In other lower stress regions, phase fragmentation could occur via fatigue mechanism after a certain number of pulse periods.

Declaration of Competing Interests

The authors declare that they have no known competing financial interests or personal relationships that could have appeared to influence the work reported in this paper.

Acknowledgements

J. Mi would like to thank the Royal Society for the Royal Society Industry Fellowship Award (2012-2016) and the EPSRC grants (EP/L019965/1 and EP/R031819/1) for supporting the research. We also would like to acknowledgethe allocation of the synchrotron X-ray beamtime at the Diamond-Manchester Imaging Branchline (I13-2) of the Diamond Light Source, UK (MT13488-1 and MT13488-2) as well as the strong technical support on computing and imaging processing by Mr C. Collins of the University of Hull High Performance Computer - Viper.

Supplementary materials

Supplementary material associated with this article can be found, in the online version, at doi:10.1016/j.actamat.2023.119593.

References

[1] C. Liu, J. Stiegler, Ductile ordered intermetallic alloys, Science 226 (4675) (1984) 636–642.
[2] E. George, M. Yamaguchi, K. Kumar, C. Liu, Ordered intermetallics, Annu. Rev. Mater. Sci. 24 (1) (1994) 409–451.
[3] S. Whang, C. Liu, D. Pope, J. Stiegler, High Temperature Aluminides and Intermetallics, Elsevier, 1990.
[4] J. Mi, Pulse External Fields Processing of Metal Alloys, Solidification Processing of Metallic Alloys Under External Fields, 2018, pp. 243–275.
[5] J. Zhao, C. Unuvar, U. Anselmi-Tamburini, Z.A. Munir, Microstructural evolution during the dissolution of nickel in liquid aluminum under the influence of an electric field, Acta Mater. 56 (8) (2008) 1840–1848.
[6] X. Li, A. Gagnoud, Z. Ren, Y. Fautrelle, R. Moreau, Investigation of thermoelectric magnetic convection and its effect on solidification structure during directional solidification under a low axial magnetic field, Acta Mater. 57 (7) (2009) 2180–2197.
[7] M. Asta, C. Beckermann, A. Karma, W. Kurz, R. Napolitano, M. Plapp, G. Purdy, M. Rappaz, R. Trivedi, Solidification microstructures and solid-state parallels: recent developments, future directions, Acta Mater. 57 (4) (2009) 941–971.
[8] Y. Yang, H. Humadi, D. Buta, B.B. Laird, D. Sun, J.J. Hoyt, M. Asta, Atomistic simulations of nonequilibrium crystal-growth kinetics from alloy melts, Phys. Rev. Lett. 107 (2) (2011), 025505.

[9] D.G. Eskin, Ultrasonic processing of molten and solidifying aluminium alloys: overview and outlook, Mater. Sci. Technol. 33 (6) (2017) 636–645.
[10] D. Du, Y. Fautrelle, Z. Ren, R. Moreau, X. Li, Effect of a high magnetic field on the growth of ternary Al-Cu-Ag alloys during directional solidification, Acta Mater. 121 (2016) 240–256.
[11] X. Li, Y. Fautrelle, Z. Ren, Influence of thermoelectric effects on the solid–liquid interface shape and cellular morphology in the mushy zone during the directional solidification of Al–Cu alloys under a magnetic field, Acta Mater. 55 (11) (2007) 3803–3813.
[12] D.G. Eskin, I. Tzanakis, F. Wang, G.S.B. Lebon, T. Subroto, K. Pericleous, J. Mi, Fundamental studies of ultrasonic melt processing, Ultrason. Sonochem. 52 (2019) 455–467.
[13] D.G. Eskin, J. Mi, Solidification Processing of Metallic Alloys Under External Fields, Springer, 2018.
[14] S. Komarov, D. Kuznetsov, Erosion resistance and performance characteristics of niobium ultrasonic sonotrodes in molten aluminum, Int. J. Refract. Met. Hard Mater. 35 (2012) 76–83.
[15] S. Amano, K. Iwai, S. Asai, Non-contact generation of compression waves in a liquid metal by imposing a high frequency electromagnetic field, ISIJ Int. 37 (10) (1997) 962–966.
[16] Y. Wang, K. Kudo, Y. Inatomi, R. Ji, T. Motegi, Growth and structure of CdZnTe crystal from Te solution with THM technique under static magnetic field, J. Cryst. Growth 275 (1–2) (2005) e1551–e1556.
[17] H.B. Hadid, D. Henry, R. Touihri, Unsteady three-dimensional buoyancy-driven convection in a circular cylindrical cavity and its damping by magnetic field, J. Cryst. Growth 180 (3–4) (1997) 433–441.
[18] Z. Lei, Z. Ren, K. Deng, W. Li, H. Wang, Experimental study on mould oscillation-less continuous casting process under high frequency amplitude-modulated magnetic field, ISIJ Int. 44 (11) (2004) 1842–1846.
[19] P. Cremer, J. Driole, Effects of the electromagnetic stirring on the removal of inclusions of oxide from liquid steel, Metall. Trans. B 13 (1) (1982) 45–52.
[20] L.B. Trindade, J.E.A. Nadalon, A.C. Vilela, M.T. Vilhena, R.B. Soares, Numerical modeling of inclusion removal in electromagnetic stirred steel billets, Steel Res. Int. 78 (9) (2007) 708–713.
[21] D. Shu, J. Mi, J. Wang, B. Sun, Modelling the electromagnetic separation of non-metallic particles from liquid metal flowing through a two-stage multichannel, ISIJ Int. 51 (1) (2011) 21–26.
[22] S. Hu, L. Hou, K. Wang, Z. Liao, W. Zhu, A. Yi, W. Li, Y. Fautrelle, X. Li, Effect of transverse static magnetic field on radial microstructure of hypereutectic aluminum alloy during directional solidification, J. Mater. Sci. Technol. 76 (2021) 207–214.
[23] H. Li, J. Zhao, Directional solidification of an Al–Pb alloy in a static magnetic field, Comput. Mater. Sci. 46 (4) (2009) 1069–1075.
[24] J. Wang, Y. Fautrelle, H. Nguyen-Thi, G. Reinhart, H. Liao, X. Li, Y. Zhong, Z. Ren, Thermoelectric magnetohydrodynamic flows and their induced change of solid–liquid interface shape in static magnetic field-assisted directional solidification, Metall. Mater. Trans. A 47 (2016) 1169–1179.
[25] X. Liu, S. Shuai, C. Huang, S. Wu, T. Hu, C. Chen, J. Wang, Z. Ren, Microstructure and mechanical properties of directionally solidified Al-rich Ni3Al-based alloy under static magnetic field, J. Mater. Sci. Technol. 110 (2022) 117–127.
[26] T. Campanella, C. Charbon, M. Rappaz, Influence of permeability on the grain refinement induced by forced convection in copper-base alloys, Scr. Mater. 49 (10) (2003) 1029–1034.
[27] T. Campanella, C. Charbon, M. Rappaz, Grain refinement induced by electromagnetic stirring: a dendrite fragmentation criterion, Metall. Mater. Trans. A 35 (10) (2004) 3201–3210.
[28] Y. Li, W. Tao, Y. Yang, Grain refinement of Al–Cu alloy in low voltage pulsed magnetic field, J. Mater. Process. Technol. 212 (4) (2012) 903–909.
[29] Q. Chen, H. Shen, Numerical study on solidification characteristics under pulsed magnetic field, Int. J. Heat Mass Transf. 120 (2018) 997–1008.
[30] K. Zhang, Y. Li, Y. Yang, Influence of the low voltage pulsed magnetic field on the columnar-to-equiaxed transition during directional solidification of superalloy K4169, J. Mater. Sci. Technol. 48 (2020) 9–17.
[31] J. Hua, Y. Zhang, C. Wu, Grain refinement of Sn–Pb alloy under a novel combined pulsed magnetic field during solidification, J. Mater. Process. Technol. 211 (3) (2011) 463–466.
[32] Y. Li, Y. Teng, X. Feng, Y. Yang, Effects of pulsed magnetic field on microsegregation of solute elements in a Ni-based single crystal superalloy, J. Mater. Sci. Technol. 33 (1) (2017) 105–110.
[33] D. Liang, Z. Liang, Q. Zhai, G. Wang, D.H. StJohn, Nucleation and grain formation of pure Al under Pulsed Magneto-Oscillation treatment, Mater. Lett. 130 (2014) 48–50.
[34] Y.Y. Gong, J. Luo, J.X. Jing, Z.Q. Xia, Q.J. Zhai, Structure refinement of pure aluminum by pulse magneto-oscillation, Materi. Sci. Eng.: A 497 (1-2) (2008) 147–152.
[35] J. Jie, S. Yue, J. Liu, D.H. StJohn, Y. Zhang, E. Guo, T. Wang, T. Li, Revealing the mechanisms for the nucleation and formation of equiaxed grains in commercial purity aluminum by fluid-solid coupling induced by a pulsed magnetic field, Acta Mater. 208 (2021), 116747.
[36] Z. Zhao, Y. Liu, L. Liu, Grain refinement induced by a pulsed magnetic field and synchronous solidification, Mater. Manuf. Process. 26 (9) (2011) 1202–1206.
[37] E. Liotti, A. Lui, R. Vincent, S. Kumar, Z. Guo, T. Connolley, I. Dolbnya, M. Hart, L. Arnberg, R. Mathiesen, A synchrotron X-ray radiography study of dendrite fragmentation induced by a pulsed electromagnetic field in an Al–15Cu alloy, Acta Mater. 70 (2014) 228–239.
[38] X. Li, Z. Ren, Y. Fautrelle, Alignment behavior of the primary Al3Ni phase in Al–Ni alloy under a high magnetic field, J. Cryst. Growth 310 (15) (2008) 3488–3497.
[39] X. Li, Y. Fautrelle, Z. Ren, Y. Zhang, C. Esling, Effect of a high magnetic field on the Al–Al3Ni fiber eutectic during directional solidification, Acta Mater. 58 (7) (2010) 2430–2441.
[40] X. Li, Z. Ren, Y. Fautrelle, A. Gagnoud, Y. Zhang, C. Esling, Degeneration of columnar dendrites during directional solidification under a high magnetic field, Scr. Mater. 60 (6) (2009) 443–446.
[41] X. Li, Y. Fautrelle, Z. Ren, R. Moreau, Formation mechanism of axial macrosegregation of primary phases induced by a static magnetic field during directional solidification, Sci. Rep. 7 (1) (2017) 1–13.
[42] J. Gao, M. Han, A. Kao, K. Pericleous, D.V. Alexandrov, P.K. Galenko, Dendritic growth velocities in an undercooled melt of pure nickel under static magnetic fields: a test of theory with convection, Acta Mater. 103 (2016) 184–191.
[43] Z. Song, E. Boller, A. Rack, P.D. Lee, B. Cai, Magnetic field-assisted solidification of W319 Al alloy qualified by high-speed synchrotron tomography, J. Alloys Compd. 938 (2023), 168691.
[44] B. Cai, A. Kao, E. Boller, O. Magdysyuk, R. Atwood, N. Vo, K. Pericleous, P. Lee, Revealing the mechanisms by which magneto-hydrodynamics disrupts solidification microstructures, Acta Mater. 196 (2020) 200–209.
[45] Z. Song, O.V. Magdysyuk, T. Sparks, Y.L. Chiu, B. Cai, Revealing growth mechanisms of faceted Al2Cu intermetallic compounds via high-speed Synchrotron X-ray tomography, Acta Mater. 231 (2022), 117903.
[46] Z. Song, O.V. Magdysyuk, L. Tang, T. Sparks, B. Cai, Growth dynamics of faceted Al13Fe4 intermetallic revealed by high-speed synchrotron X-ray quantification, J. Alloys Compd. 861 (2021), 158604.
[47] J. Cao, S. Shuai, C. Huang, T. Hu, C. Chen, J. Wang, Z. Ren, 4D synchrotron X-ray tomographic study of the influence of transverse magnetic field on iron intermetallic compounds precipitation behavior during solidification of Al–Si–Fe alloy, Intermetallics 143 (2022), 107471.
[48] P. Mikolajczak, L. Ratke, Effect of stirring induced by rotating magnetic field on β-Al5FeSi intermetallic phases during directional solidification in AlSi alloys, Int. J. Cast Met. Res. 26 (6) (2013) 339–353.
[49] T. Manuwong, W. Zhang, P.L. Kazinczi, A.J. Bodey, C. Rau, J. Mi, Solidification of Al alloys under electromagnetic pulses and characterization of the 3D microstructures using synchrotron X-ray tomographyMetall, Mater. Trans. A: Phys. Metall. Mater. Sci. 46 (7) (2015) 2908–2915.
[50] K. Xiang, S. Huang, J. Mi, Characterisations of the Al-Mn intermetallic phases formed under pulse magnetic fields solidification, in: IOP Conference Series: Materials Science and Engineering, IOP Publishing, 2023, 012004.
[51] B. Koe, C. Abraham, C. Bailey, B. Greening, M. Small, T. Connolley, J. Mi, A novel electromagnetic apparatus for in-situ synchrotron X-ray imaging study of the separation of phases in metal solidification, HardwareX 7 (2020), e00104.
[52] W. Du, In-situ synchrotron X-ray imaging and tomography studies of the evolution of solidification microstructures under pulse electromagnetic fields, University of Hull, 2018.
[53] T. Manuwong, Solidification of metal alloys in pulse electromagnetic fields, University of Hull, 2015.
[54] N. Wadeson, M. Basham, Savu: a Python-based, MPI framework for simultaneous processing of multiple, N-dimensional, large tomography datasets. arXiv preprint, 2016. arXiv:1610.08015.
[55] D. Kazantsev, N. Wadeson, M. Basham, High performance Savu software for fast 3D model-based iterative reconstruction of large data at Diamond Light Source, SoftwareX 19 (2022), 101157.
[56] I. Arganda-Carreras, V. Kaynig, C. Rueden, K.W. Eliceiri, J. Schindelin, A. Cardona, H.Sebastian Seung, Trainable Weka segmentation: a machine learning tool for microscopy pixel classification, Bioinformatics 33 (15) (2017) 2424–2426.
[57] M.D. Abràmoff, P.J. Magalhães, S.J. Ram, Image processing with Image, J. Biophotonics Ternational 11 (7) (2004) 36–42.
[58] I. Levner, H. Zhang, Classification-driven watershed segmentation, IEEE Trans. Image Process. 16 (5) (2007) 1437–1445.
[59] G. Dulikravich, Electro-magneto-hydrodynamics and solidification, Rheol. Ser. 8 (1999) 677–716.
[60] G. May, G. Chadwick, The fatigue behaviour of the aligned Al-Al3Ni eutectic alloy, Metal Sci. J. 7 (1) (1973) 20–25.
[61] C. Puncreobutr, A. Phillion, J. Fife, P. Rockett, A. Horsfield, P. Lee, In situ quantification of the nucleation and growth of Fe-rich intermetallics during Al alloy solidification, Acta Mater. 79 (2014) 292–303.
[62] X. Li, Y. Fautrelle, Z. Ren, Morphological instability of cell and dendrite during directional solidification under a high magnetic field, Acta Mater. 56 (13) (2008) 3146–3161.
[63] C.W. Lan, C.J. Shih, Phase field simulation of non-isothermal free dendritic growth of a binary alloy in a forced flow, J. Cryst. Growth 264 (1-3) (2004) 472–482.
[64] C. Lan, C. Hsu, C. Liu, Efficient adaptive phase field simulation of dendritic growth in a forced flow at low supercooling, J. Cryst. Growth 241 (3) (2002) 379–386.
[65] Y. Teng, Y. Li, X. Feng, Y. Yang, Effect of rectangle aspect ratio on grain refinement of superalloy K4169 under pulsed magnetic field, Acta Metall. Sin 51 (7) (2015) 844–852.
[66] N. Balasubramani, Y. Xu, Y. Zhang, Q. Zhai, G. Wang, D. StJohn, M. Dargusch, Investigating the grain refinement mechanisms of pulsed electric current,

ultrasonic and melt stirring solidification of pure aluminium, JOM 73 (12) (2021) 3873–3882.
[67] N. Balasubramani, J. Venezuela, D. StJohn, G. Wang, M. Dargusch, Review of origin of equiaxed grains during solidification under mechanical stirring, vibration, electromagnetic, electric-current, and ultrasonic treatments, J. Mater. Sci. Technol. (2022).
[68] X. Wang, H. Wang, C. Zou, Z. Wei, Y. Uwatoko, J. Gouchi, D. Nishio-Hamane, H. Gotou, The effects of high pressure and superheating on the planar growth of Al3Ni phase in hypo-peritectic Al-30wt% Ni alloy, J. Alloys Compd. 772 (2019) 1052–1060.
[69] X. Wang, Z. Chen, D. Dong, D. Zhu, H. Wang, Z. Wei, Study on the phase selection and debye temperature of hyper-peritectic Al-Ni alloy under high pressure, Metals 11 (1) (2021) 84.